



An ultrathin carbon layer activated CeO₂ heterojunction nanorods for photocatalytic degradation of organic pollutants



Kaihang Ye^a, Ya Li^b, Hao Yang^a, Mingyang Li^a, Yongchao Huang^{b,*}, Shanqing Zhang^{c,*}, Hongbing Ji^{a,*}

^a Fine Chemical Industry Research Institute, School of Chemistry, Sun Yat-Sen University, Guangzhou, 510275, Guangdong, China

^b Institute of Environmental Research at Greater Bay Area, Key Laboratory for Water Quality and Conservation of the Pearl River Delta, Ministry of Education, Guangzhou University, Guangzhou, 510006, China

^c Country Centre for Clean Environment and Energy, School of Environment and Science, Gold Coast Campus, Griffith University, Australia

ARTICLE INFO

Keywords:
Photocatalysis
Carbon layer
CeO₂ heterojunction
Water purity
Oxygen species

ABSTRACT

Designing and constructing effective and stable photocatalysts is the major challenge in the development of photocatalysis. Herein, we demonstrate a conceptual strategy to effectively improve the charge separation in a ternary material system (CeO₂/C/SnS₂), by introducing ultrathin carbon layer between CeO₂ nanorods and SnS₂ particles as a conductive electron transport “highway”. Such ternary CeO₂/C/SnS₂ gives rise to a largely enhanced photocatalytic removal performance of phenol (100%, 60 min), comparing with CeO₂/SnS₂ (50%) and CeO₂ (20%). Experimental results reveal that carbon layer acts as a high work function, superior electron mobility accepts and enables a fast transportation, accelerating the photocatalytic degradation performance of phenol. Our design introduces material components to provide a dedicated charge-transport pathway, conquering the materials’ intrinsic properties, providing a new perspective for water purity.

1. Introduction

Photocatalysis has been considered as one of the most tempting solutions to allay the environmental problem and energy issues, which directly converts the solar light into chemical energy [1–12]. There are three central steps during the photocatalytic process: 1) harvesting light to produce electron-hole pairs, 2) charge carriers separation and diffusion to the photocatalyst surface, 3) reduction and oxidation reaction on the catalyst surface [13–15]. Until now a series of strategies have been performed to modify the photocatalysts based on the above three aspects, such as doping, defects engineering, morphology tuning, hybridization and so on [16–20]. Among which, constructing hybridization has been regarded as an effective methodology to improve the light absorption, charge separation and interfacial redox reaction.

In hybridization systems, the formation of the contact interface has a significant impact on the resistance level of electron transfer [21–23]. The design of contact interface would affect the charge transfer in composites systems [24]. The chemical contact is the main contact mode to form a tight interface between the materials for effective carrier transfer, using one photocatalyst as a substrate and loads another photocatalyst onto the surface of the former by surface conjugation via chemical bonding, such as CeO₂/CeN composite [25], ZnO/BiOI [26],

BiVO₄/Bi₂O₂CO₃ [27], Co₃O₄/BiVO₄ [28], Pd/BiOI/MnO_x [29] and so on [8,30–32]. The contact interface between the materials could effectively improve the transfer and separation of photo-induced charge carriers during the photocatalytic process due to intense physical and electronic coupling effects (an internal electric field induced from band bending) [33,34]. This phenomenon inspires us that speeding up the charge carriers in the contact interface to improve the separation of photo-induced charge carriers, such as, building the “bridge” between two materials to enhance the charges transfer? In order to verify this hypothesis, we construct CeO₂/C/SnS₂ composites, which carbon layer between two semiconductors as electron transport “highway”. CeO₂ has recently captured our interest due to its redox properties and outstanding optical properties [18,35–37]. Carbon is used as the “bridge” due to its good ability to functionalize easily with other materials, excellent conductivity, high strength and high chemical stability [38]. Additionally, SnS₂ has a wide absorption and good conductivity, utilizing visible light effectively. Therefore, compositing of CeO₂ and SnS₂ to boost the carrier transfer property, improving the photocatalysis. More importantly, carbon layer provides a conductive electron transport “highway” between CeO₂ and SnS₂, improving the photocatalytic performance.

Herein, we reported the design and fabrication of carbon layer on

* Corresponding authors.

E-mail addresses: huangych@gzhu.edu.cn (Y. Huang), s.zhang@griffith.edu.au (S. Zhang), jihb@mail.sysu.edu.cn (H. Ji).

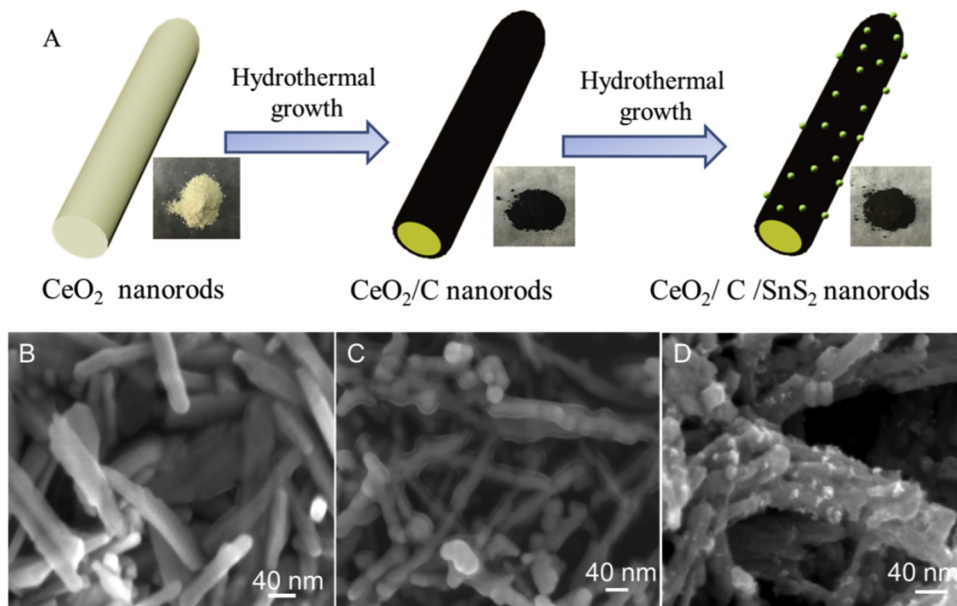


Fig. 1. (A) Schematic illustration for the fabrication of CeO₂/C/SnS₂ nanorods (inset is the sample photos); SEM images of (B) CeO₂ nanorods, (C) CeO₂/C nanorods and (D) CeO₂/C/SnS₂ nanorods.

the surface of CeO₂ nanorods, followed by a subsequent hydrothermal method of SnS₂, which exhibited largely improved photocatalysis. The hierarchical CeO₂/C/SnS₂ with a ternary structure was demonstrated with fine control over the composition and morphology; the C and SnS₂ were uniformly dispersed onto the surface of CeO₂ nanorods. The prepared ternary nanorods showed excellent performance for waste water treatment and satisfactory stability (no any decay after 5 cycles). The experimental results reveal that the photocatalytic performance of CeO₂ heterojunction is attributed to the synergistic effect of the superior charge separation efficiency facilitated by carbon layer.

2. Experimental

2.1. Synthesis of CeO₂/C/SnS₂ nanorods

In a typical process, CeO₂ nanorods were first prepared according to our previous work [25]. 0.2 g CeO₂ was dispersed into the 30 mL deionized water with ultrasound for 1 h. After that, 0.1, 0.15, 0.2 M glucose was added to the above solution and stirred constantly for 30 min, respectively. Then the solution was transferred into a 50 mL Teflon-lined stainless-steel autoclave and maintained at 180 °C for 3 h. The obtained products were centrifuged and washed with deionized water and ethanol several times. The CeO₂/C nanorods were obtained by annealing the product in N₂ gas at temperatures (800 °C) for 1 h at a ramp rate of 10 °C min⁻¹ and the products were denoted as CeO₂/C_{0.1}, CeO₂/C_{0.15} and CeO₂/C_{0.2}, respectively. CeO₂/C/SnS₂ nanorods were obtained by the following method: 0.2 g CeO₂/C was dispersed into the 60 mL ethanol solution with 0.001 M SnCl₄ and 0.003 M thiouacetamide. And the solution was maintained at 75 °C for 3 h. The obtained products were centrifuged and washed with deionized water and ethanol several times.

2.2. Characterization

Field emission scanning electron microscope (JSM-6330 F), X-ray Diffractometer (D8 ADVANCE), X-ray photoelectron spectroscopy (ESCALab250), Transmission electron microscopy (JEM2010-HR) and specific surface area (ASAP 2020 V3..03 H), UV – vis – NIR spectrophotometer (UV – vis – NIR, Shimadzu UV-2450) and Room-temperature photoluminescence spectra (FLS920, EDINBURGH) were used

to characterize the morphology and structure of all the catalysts. The reactive species in photocatalysis were performed by electron spin resonance test with ESR-DMPO, using the X-band (9.45 GHZ) with 5.00 G modulation amplitude and a magnetic field modulation of 100 kHz. The electrochemical tests were carried out with a CHI 660 C electrochemical station in a standard three electrode configuration. The illumination source was AM 1.5 G solar simulator [Newport, LCS 100 94011A (class A,)] directed at the quartz PEC cell (100 mW cm⁻²). We prepared the working electrode (photoanode) as follows: 20 mg of sample was mixed with 2 mL ethyl alcohol to form slurry then coated onto a 1 cm × 1 cm fluorine-doped tin oxide (FTO) glass substrate and dried at 80 °C for 10 h. The total organic carbon (TOC) concentration was determined by a TOC auto analyzer (Acquray TOC seri).

All calculations have been carried out with the Vienna ab initio Simulation Package (VASP). 3D periodic boundary conditions were applied to simulate the infinitely large systems. A 20 Å vacuum space between sheets was set to prevent the interaction between two membrane layers. The Brillouin zone of the fibre was sampled by 1 × 3 × 1 k-points. The electronic structure of the system was treated using the generalized gradient approximation with the PBE functional. The van der Waals interactions were added to the standard DFT description by Grimme's D2 scheme.

2.3. Photocatalytic activity measurements

Catalyst (0.05 g) was added to a 100 mL 10 mg L⁻¹ phenol solution. Firstly, the solution was magnetically stirred for 60 min. A 300 W Xe lamp with a 420 nm UV light cut filter was used as the light source and the distance was about 20 cm above the solution. 3.0 mL reactive solution was taken out after the light irradiation at different time. UV-vis spectrophotometer was used to test the residual dyes concentration with the 655 nm absorbance for phenol. The photocatalytic efficiency was calculated by the C/C₀ × 100% (C is the final dyes concentrations and C₀ is the initial concentration of dyes).

3. Results and discussion

3.1. Synthesis and characterization of all the catalysts

As a typical presentation, CeO₂ nanorods are chosen as a prototype

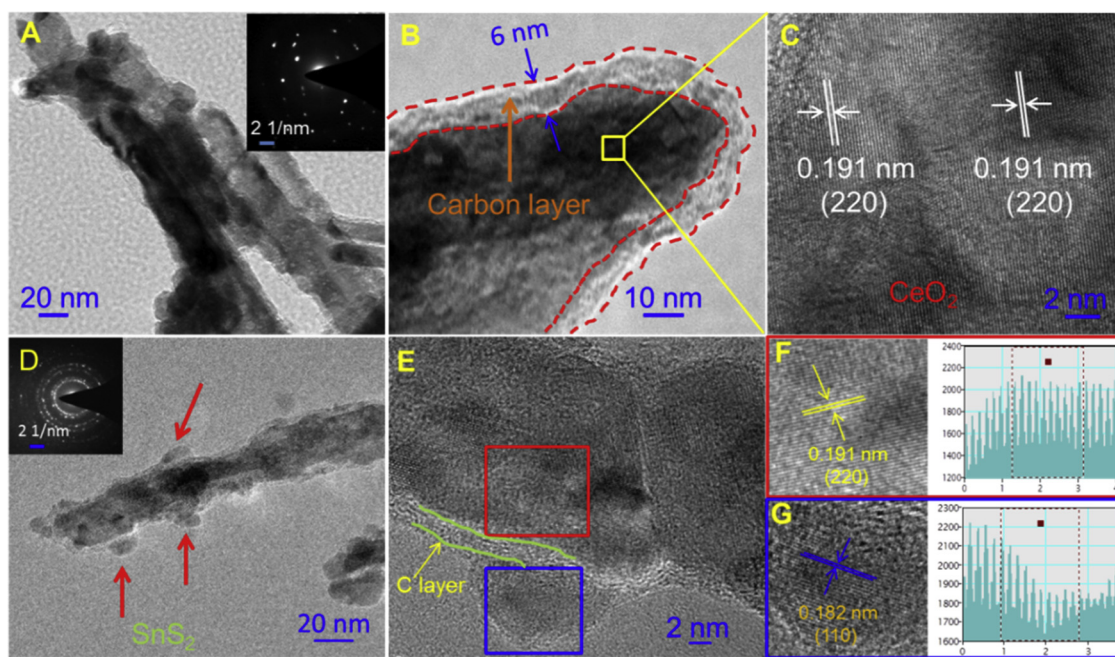


Fig. 2. (A–C) TEM images and HRTEM image of CeO₂/C nanorods; (D, G, F, G) TEM images and HRTEM image of CeO₂/C/SnS₂ nanorods.

for the investigation of building carbon “highway” between two materials to improve the charges transfer due to its redox properties and outstanding optical properties [18,35–37]. Fig. 1A shows the fabrication process of CeO₂/C/SnS₂ nanorods. CeO₂ nanorods are firstly prepared via a previously reported hydrothermal method, with a diameter range from 30 nm to 50 nm (Fig. 1B). Subsequently, C layer is coated onto CeO₂ nanorods via hydrothermal method and followed by an annealing process in N₂ [39]. As displayed in Fig. 1C, carbon layer irregularly coated on CeO₂ surface. Finally, SnS₂ nanoparticles with an average size of 10 nm are deposited on the surface of CeO₂/C (Fig. 1D). CeO₂/SnS₂ nanorods are synthesized for compared without C “bridge” between two materials (Fig. S1). The Brunauer-Emmett-Teller (BET) surface area values are 45.2 m² g⁻¹, 86.8 m² g⁻¹, 75.2 m² g⁻¹ and 78.8 m² g⁻¹ for CeO₂, CeO₂/C, CeO₂/SnS₂ and CeO₂/C/SnS₂, respectively (Fig. S2). C layer covering on the surface of CeO₂ nanorods can change the polished surface of CeO₂, making the coarser surface, suggesting that carbon layer can improve the BET surface area.

The detailed morphology of as-prepared catalysts is further detected by transmission electron microscopy (TEM) measurement. Fig. 2A–C displays the TEM images of CeO₂/C nanorods. It can be observed that amorphous C layer (about 10 nm) coated onto CeO₂ nanorods and the lattice spacing of 0.191 nm is indexed to the (220) plane of cubic structure type CeO₂. The SAED reveals that CeO₂ is a single crystal structure (inset in Fig. 2A). In addition, Fig. 2D displays the TEM images of CeO₂/C/SnS₂ nanorods. The SAED reveals that the sample is polycrystalline structure. HRTEM image confirms that multilayered structure is successfully constructed, carbon layer insets into the CeO₂ and SnS₂ (Fig. 2E). And the corresponding lattice fringes of 0.191 nm and 0.182 nm are indexed to the (220) and (110) planes of CeO₂ and SnS₂, respectively (Fig. 2F and 2G). The TEM results are in line with the results of SEM, revealing that the “carbon highway” is successfully constructed between CeO₂ and SnS₂.

The phase structure and composition of these samples are characterized by X-ray diffraction measurement (XRD), Raman and X-ray photoelectron spectroscopy (XPS) test [40]. As displayed in Fig. 3A, four sharp reflections located at 28.3°, 33.1°, 47.5° and 56.4° correspond to the (111), (200), (220) and (311) diffraction peaks of cubic structure type CeO₂ (JCPDS No 34-0394), respectively [35]. No other reflection peaks of carbon are observed for CeO₂/C nanorods, which is

mainly due to the amorphous form or small loading amount. After the loading of SnS₂, three reflection peaks are observed, indexing to the hexagonal SnS₂ (JCPDS No 21-1231). Raman spectra show the vibrational mode of cubic CeO₂ at 465 cm⁻¹ [35]. Two bands located at 1359 cm⁻¹ (D band) and 1586 cm⁻¹ (G band) are observed in CeO₂/C and CeO₂/C/SnS₂, indicating the presence of carbon (Fig. 3B) [41]. Moreover, a peak located at 308 cm⁻¹ in CeO₂/SnS₂ and CeO₂/C/SnS₂ is attributed to the A_{1g} mode of SnS₂ according to the previous report [42]. CeO₂ signal cannot be detected over CeO₂/SnS₂ and CeO₂/C/SnS₂ due to the engineering deficiency. C 1s XPS spectra also demonstrate the existence of C layer between CeO₂ and SnS₂ (Fig. 3C). Obviously, a peak at 288.1 eV arises in the spectrum of CeO₂/C and CeO₂/C/SnS₂, demonstrating the presence of C layer [43]. The composition of SnS₂ is also confirmed by the XPS spectra (Fig. S4). The percentage of every component (Ce: O: C: Sn: S) in CeO₂/C/SnS₂ is about 20.21% : 40.64% : 31.84% : 2.49% : 4.82% (Table S1). Furthermore, the optical properties of these samples are investigated by UV-vis diffuse reflectance spectroscopy. CeO₂ exhibits a strong absorption in UV light region with a steep absorption edge at approximately 500 nm (Fig. 3D), and its band gap is calculated to be 2.5 eV (Fig. S5). After introduction of C layer and SnS₂, absorbance in visible light region increases gradually, owing to the visible light absorption of C or SnS₂. The above results demonstrate the success of building carbon “bridge” between CeO₂ and SnS₂.

3.2. Photocatalytic activity and mechanism discussion

To confirm our proposal that carbon “bridge” in catalysts could improve the photocatalytic performance, CeO₂/C/SnS₂ nanorods and contrast samples are performed for photodegradation of phenol in waste water. Phenol, a colorless organic in aqueous solution as a typical organic dye, can eliminate the effect of photosensitization on the enhanced visible light driven photodegradation [44,45]. As shown in Fig. 4A, in the absence of photocatalysts, the degradation efficiency of phenol could be ignored within the test period under the visible light irradiation, suggesting that photolysis of phenol is negligible. We also compare TiO₂ with all the catalysts. The photodegradation performance of TiO₂ could be ignored under the visible light irradiation. The photocatalytic performance of CeO₂/C/SnS₂ catalyst is superior to that of TiO₂. The degradation efficiency of CeO₂/C/SnS₂ nanorods increases

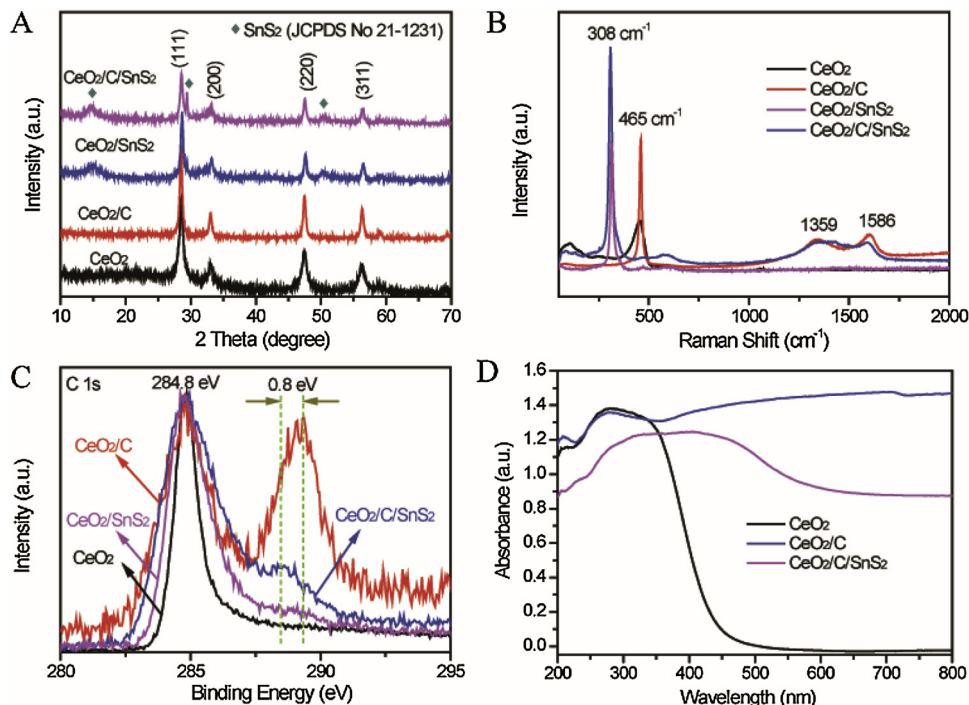


Fig. 3. (A) XRD patterns, (B) Raman spectra, (C) C 1s XPS spectra and (D) UV-vis spectra of CeO_2 , CeO_2/C , $\text{CeO}_2/\text{SnS}_2$ and $\text{CeO}_2/\text{C}/\text{SnS}_2$.

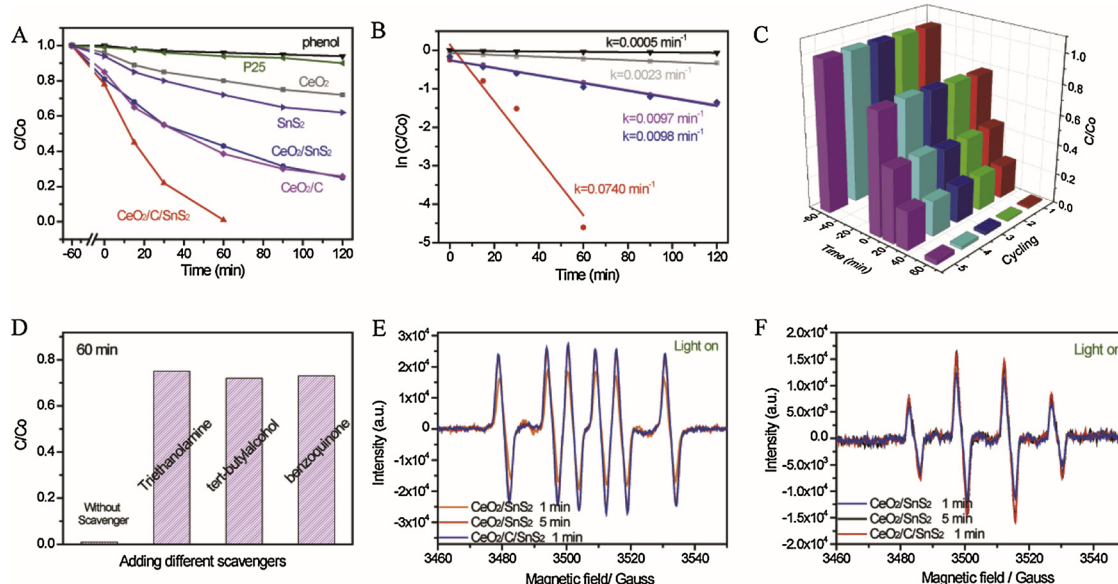


Fig. 4. Under visible light irradiation ($\geq 420 \text{ nm}$): (A) Photocatalytic performance, (B) Reaction kinetic of degradation of phenol with different catalysts. (C) Photocatalytic stability of $\text{CeO}_2/\text{C}/\text{SnS}_2$. (D) Performance of phenol degradation with $\text{CeO}_2/\text{C}/\text{SnS}_2$ and different scavengers. ESR measurement results of (E) DMPO- O_2^- , (F) DMPO-OH.

more quickly with time of visible light irradiation than that for $\text{CeO}_2/\text{SnS}_2$, CeO_2 and SnS_2 . The degradation rate of phenol with the exist $\text{CeO}_2/\text{C}/\text{SnS}_2$ nanorods reaches 99% after 60 min, but only less than 50% of phenol are degraded with $\text{CeO}_2/\text{SnS}_2$, 20% with pristine CeO_2 nanorods and 30% with pristine SnS_2 . This result reveals that C “bridge” between two semiconductors can enhance the photocatalytic performance, proving our hypothesis. Furthermore, the kinetic behaviors can be indexed to pseudo-first-order kinetics, which is displayed in Fig. 4B. $\text{CeO}_2/\text{C}/\text{SnS}_2$ nanorods display the best reaction rate constant, suggesting that $\text{CeO}_2/\text{C}/\text{SnS}_2$ nanorods is an excellent photocatalyst. The effect of C layer thickness is studied for the photocatalytic performance (Fig. S6), displaying the performance of degradation

phenol with different C layer thickness catalysts. The performances are almost the same under the visible light irradiation, revealing that the effect of C layer thickness can be ignored. In addition, to confirm the stability of the high photocatalytic activity of $\text{CeO}_2/\text{C}/\text{SnS}_2$ nanorods, recycling tests for the photodegradation of phenol are performed (Fig. 4B). The photodegradation ability remains constant over 5 consecutive cycles, with strong resistance to composition changes and morphology (Fig. S7), indicating that $\text{CeO}_2/\text{C}/\text{SnS}_2$ nanorods are stable under visible light irradiation. Furthermore, Table S2 displays the efficiency of the phenol degradation under visible light after 60 min. It could be seen that the photodegradation efficiency of phenol to CO_2 is about 91.4% under visible light irradiation, suggesting that most

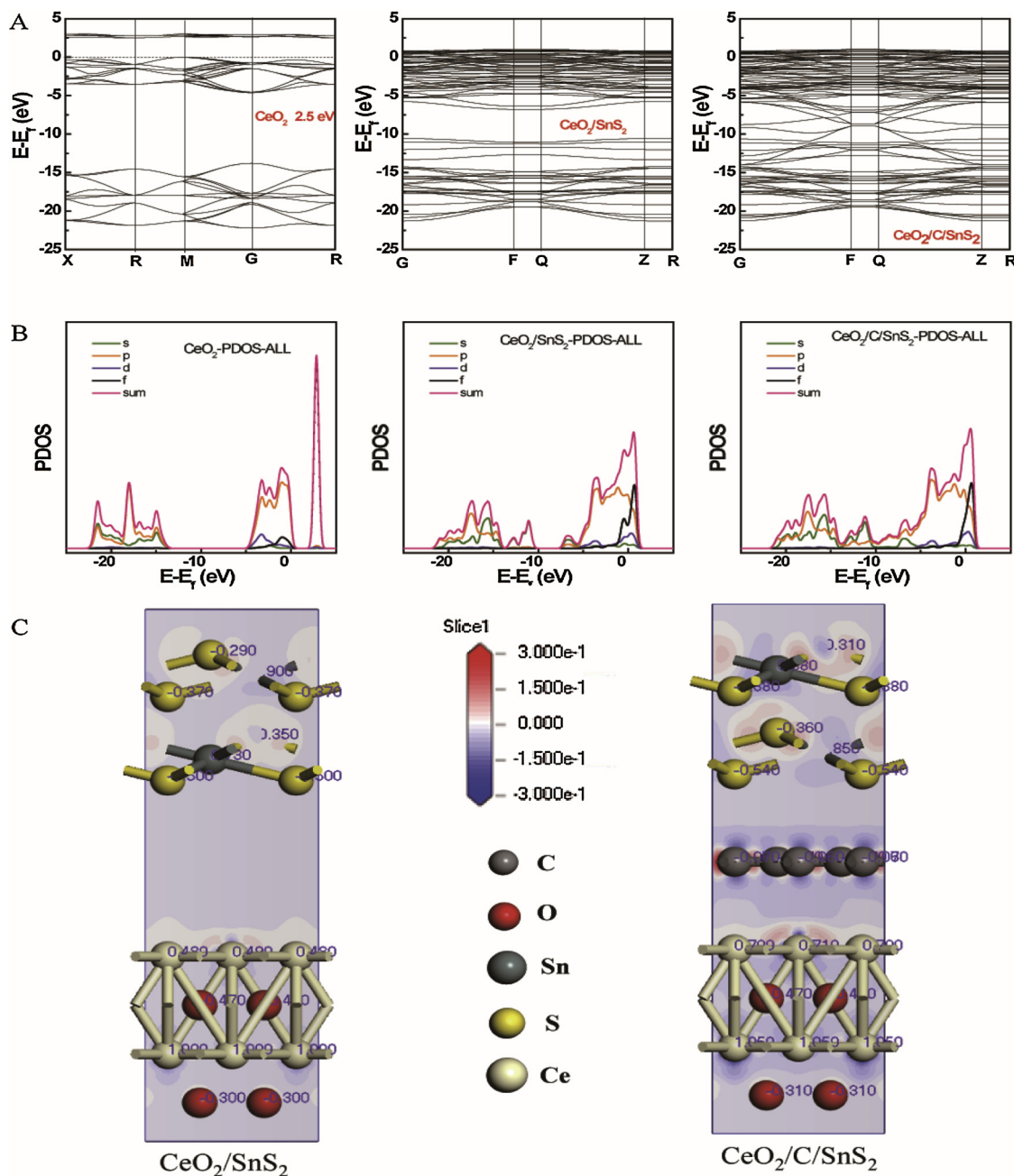


Fig. 5. Density functional theory (DFT) calculations of $\text{CeO}_2/\text{SnS}_2$ and $\text{CeO}_2/\text{C/SnS}_2$: (A) Band structure; (B) Density of states (DOS); (C) charge-density collected for different bonds, respectively.

phenol is decomposed into CO_2 and H_2O .

During the photocatalytic process, hydroxyl radical, h^+ and superoxide radical display an important role on the performance [46,47]. Therefore, we use scavengers to detect the active species in $\text{CeO}_2/\text{C/SnS}_2$ degradation of phenol (triethanolamine as h^+ scavenger, tert-butylalcohol as hydroxyl radical scavenger and benzoquinone as superoxide radical scavenger). Fig. 4D reveals the photocatalytic activities of phenol degradation with different scavengers under the visible light irradiation at 60 min. The photocatalytic degradation efficiency are obviously decreased after adding scavengers, suggesting that hydroxyl radical, h^+ and superoxide radical are produced and assume an important role during the photocatalytic degradation process. Furthermore, ESR measurements with 5, 5-dimethyl-l-pyrroline N-oxide (DMPO) are performed to provide the direct evidences for the existence of active species [44]. Six typical peaks can be observed with DMPO-

$\cdot\text{O}_2^-$ for $\text{CeO}_2/\text{SnS}_2$ and $\text{CeO}_2/\text{C/SnS}_2$, revealing that $\cdot\text{O}_2^-$ is generated during the photocatalytic degradation process. In the same case, four representative ESR peaks of $\cdot\text{OH}$ are detected with visible light irradiation, suggesting the existent of $\cdot\text{OH}$ in the process. It is important that the intensity of ESR peaks for $\text{CeO}_2/\text{C/SnS}_2$ are much higher than that of $\text{CeO}_2/\text{SnS}_2$ with the same irradiation time, suggesting that $\text{CeO}_2/\text{C/SnS}_2$ produces more active species and then improves the photocatalytic performance.

3.3. Effect of “Carbon Bridge” on the charge transfer between CeO_2 and SnS_2

Density functional theory (DFT) calculations are performed to study the role of carbon in constructing the “bridge” between CeO_2 and SnS_2 [48]. The DFT calculations are carried out with the Vienna ab initio

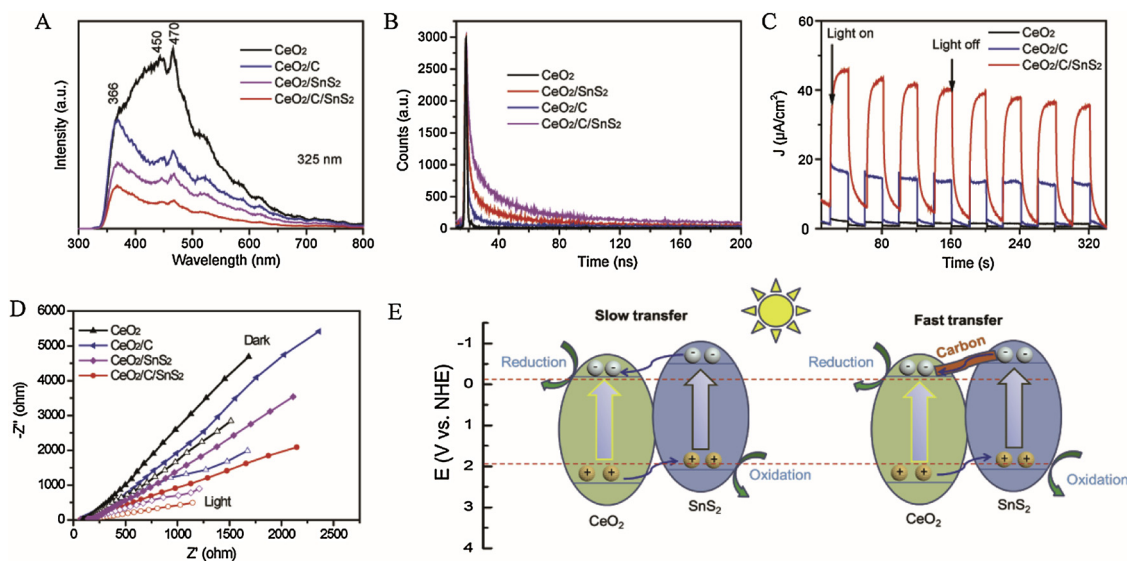


Fig. 6. (A) PL spectra (325 nm excitation wavelength), (B) Time-resolved photoluminescence spectra, (C) Photocurrents responses and (D) EIS Nyquist plots of CeO₂, CeO₂/C, CeO₂/SnS₂ and CeO₂/C/SnS₂, (E) Schematic for the proposed mechanism of heterojunction photocatalysts.

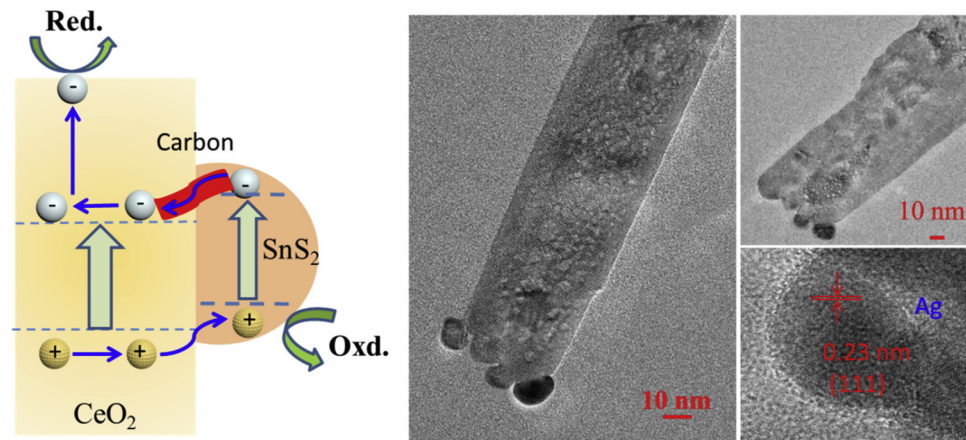


Fig. 7. Schematic for the proposed mechanism of electrons and TEM image of Ag/CeO₂.

Simulation Package (VASP) (detailed in the experimental section). Fig. 5A shows the calculated band structure of CeO₂, CeO₂/SnS₂ and CeO₂/C/SnS₂. It could be seen that the band gap of CeO₂/C/SnS₂ is much smaller than those of CeO₂, CeO₂/SnS₂, which is accorded with results of UV-vis. In order to better illustrate the role of each element in the system, the partial and total density of states (DOS) are also calculated [49]. As displayed in Fig. 5B, the valence band of CeO₂/SnS₂ and CeO₂/C/SnS₂ both shift to higher energy levels compared with CeO₂, while the conduction band shift to lower energy levels. This suggests that the photoinduced charge transfer in CeO₂/SnS₂ in followed the traditional heterojunction-type way. As shown in the optimized in Fig. 5C, the charge-density of CeO₂/SnS₂ and CeO₂/C/SnS₂ is difference. The carbon bridge could enhance the charge transfer between CeO₂ and SnS₂.

The fluorescence behavior is originated from the recombination of photoinduced electron-hole pairs, which can reflect the separation, migration and transfer of photogenerated charge carriers in semiconductors [50,51]. As shown in Fig. 6A, CeO₂ nanorods display strong PL emission peaks at 450 and 470 nm. This is due to the bandgap transition and the charge transfer transition of oxygen vacancy trapper electrons, respectively. The PL intensity of these two peaks decreases sharply after the loading of C or SnS₂, and further declines in the ternary CeO₂/C/SnS₂ system. This phenomenon indicates a significantly suppressed recombination of photogenerated charge carriers,

which benefits the electron-hole separation. The result suggests that C “bridge” between CeO₂ and SnS₂ can effectively separate the photogenerated charge carriers. That is to say, a longer life of photogenerated charge carriers will exist. Time resolved PL spectroscopy is performed to detect the dynamics of photogenerated charge carriers [52], which is shown in Fig. 6B. According to triple-exponential fitting of the emission decay curves (Table S3), the fluorescence lifetime values for CeO₂, CeO₂/C, CeO₂/SnS₂ and CeO₂/C/SnS₂ are 0.73, 0.99, 1.37 and 2.15 ns, respectively. The prolonged fluorescence lifetime of CeO₂/C/SnS₂ is related to a long life of electrons at excited state, corresponding to the migration and surface reaction of photogenerated charge carriers [53]. Fig. 6C displays a prompt and reproducible photocurrent response with respect to the ON-OFF cycles of the irradiation signal. The current density of CeO₂/C/SnS₂ is much higher than those of CeO₂ and CeO₂/C, suggesting the fast photoelectrons transfer, which is highly in accordance with the results of PL [36]. It further confirms that C “bridge” could effectively separate the photogenerated charge carriers for CeO₂/C/SnS₂. However, the photocurrent value of CeO₂/C/SnS₂ decay is due to that the catalysts detached from the electrode. Charge transport behavior in these samples is investigated by electrochemical impedance spectroscopy (EIS). As shown in Fig. 6D, the CeO₂/C/SnS₂ displays the smallest charge transfer resistance in dark or under visible light irradiation, suggesting the fastest charge transport kinetics [54,55]. According to the above analysis, building the “C bridge” between CeO₂

and SnS_2 can improve the charges transfer, enhancing the photocatalytic performance.

Based on the above results, a possible photocatalytic mechanism is proposed in Fig. 6E. CeO_2 nanorods display relatively low performance due to the low light absorption efficiency and transfer of charge carriers. After compositing with SnS_2 nanoparticles, the resulting $\text{CeO}_2/\text{SnS}_2$ enhances photocatalytic performance. Photo-induced electrons from SnS_2 move to CeO_2 , while holes from CeO_2 transfer to SnS_2 based on the potential difference of CeO_2 ($E_g = 2.5 \text{ eV}$, $E_{CB} = -0.19 \text{ eV}$, $E_{VB} = 2.31 \text{ eV}$) and SnS_2 ($E_g = 2.05 \text{ eV}$, $E_{CB} = -0.49 \text{ eV}$, $E_{VB} = 1.56 \text{ eV}$) (Figure S8), the values are closed to the reported [37,56]. Therefore, the heterojunction structure utilizes more incoming light and enhances the charge separation across the junction structure, improving the photocatalytic performance of $\text{CeO}_2/\text{SnS}_2$. The carbon layer between $\text{CeO}_2/\text{SnS}_2$ could improve the photocatalytic performance due to that carbon layer behaving as an electron conductor to enhance the separation of electron-hole, speeding up the electron transmission from the conduction band of SnS_2 to the conduction band of CeO_2 , providing a conductive electron transport "highway". The electrons in CeO_2 nanorods are suggested to transfer along with the nanorods orientation, while the holes will transfer toward the lateral direction [57], which is verified by the results that the photoconductive deposition of silver ions is observed on the top side of the CeO_2 nanorods (Fig. 7). The photo-generated holes undergo a very short transfer distance in the lateral direction for better charge separation. Therefore, the $\text{CeO}_2/\text{C}/\text{SnS}_2$ has the advantages of enhanced light absorption, large contact area, abundant hetero-interfaces and rapid charge separation and transport, favoring the migration and separation of photogenerated electron-hole pairs, and contributing to the efficient photocatalytic performance for water treatment.

4. Conclusions

In summary, ternary $\text{CeO}_2/\text{C}/\text{SnS}_2$ nanorods were successfully prepared and confirmed through systematic materials characterization. The resulting ternary $\text{CeO}_2/\text{C}/\text{SnS}_2$ demonstrated significantly improved efficiency in photocatalytic degradation of phenol and high stability, which is superior to the reported Ce-based photocatalysts. The deep insight into the mechanism for the boosted photocatalytic performance has also been researched systematically. The improved light harvesting, fast charge transfer and efficient separation of photogenerated electron-hole pairs along with introducing ultrathin carbon layer between CeO_2 nanorods and SnS_2 particles as a conductive electron transport "highway" contribute to the photocatalytic degradation of phenol in waste water. Therefore, our results reveal remarkable strategies for constructing efficiency photocatalyst for practical sun-light-responded photocatalytic waste water treatment.

Declaration of Competing Interest

The authors declare that they have no known competing financial interests or personal relationships that could have appeared to influence the work reported in this paper.

Acknowledgements

We sincerely thanks the following funds support: Natural Science Foundation of China (21773315), Natural Science Foundation of Guangdong Province (2017A030313055), the Pearl River S&T Nova Program of Guangzhou (201906010024), Innovative School Project of Guangzhou University (2823010936) and the Science Starting Foundation of Guangzhou University (69-18ZX10301), the China Postdoctoral Science Foundation (2018M640847, 2019T120764).

Appendix A. Supplementary data

Supplementary material related to this article can be found, in the online version, at doi:<https://doi.org/10.1016/j.apcatb.2019.118085>.

References

- [1] J. Di, C. Zhu, M. Ji, M. Duan, R. Long, C. Yan, K. Gu, J. Xiong, Y. She, J. Xia, H. Li, Z. Liu, *Angew. Chem.* 130 (2018) 15063–15067.
- [2] D.J. Martin, G. Liu, S.J.A. Moniz, Y. Bi, A.M. Beale, J. Ye, J. Tang, *Chem. Soc. Rev.* 44 (2015) 7808–7828.
- [3] J. Di, J. Xia, M.F. Chisholm, J. Zhong, C. Chen, X. Cao, F. Dong, Z. Chi, H. Chen, Y.-X. Weng, J. Xiong, S.-Z. Yang, H. Li, Z. Liu, S. Dai, *Adv. Mater.* 31 (2019) 1807576–1807584.
- [4] Y. Sun, S. Gao, F. Lei, C. Xiao, Y. Xie, *Acc. Chem. Res.* 48 (2015) 3–12.
- [5] J. Li, X. Wu, W. Pan, G. Zhang, H. Chen, *Angew. Chem.* 57 (2018) 491–495.
- [6] S. Chen, Y. Qi, T. Hisatomi, Q. Ding, T. Asai, Z. Li, S.S.K. Ma, F. Zhang, K. Domen, C. Li, *Angew. Chem.* 54 (2015) 8498–8501.
- [7] C. Liu, D. Kong, P.-C. Hsu, H. Yuan, H.-W. Lee, Y. Liu, H. Wang, S. Wang, K. Yan, D. Lin, P.A. Maraccini, K.M. Parker, A.B. Boehm, Y. Cui, *Nature Nanotechnol.* 11 (2016) 1098–1104.
- [8] X.Z. Li, H. Liu, L.F. Cheng, H.J. Tong, *Environ. Sci. Technol.* 37 (2003) 3989–3994.
- [9] W. Wang, G. Li, T. An, D.K.L. Chan, J.C. Yu, P.K. Wong, *Appl. Catal. B Environ.* 238 (2018) 126–135.
- [10] J. Pan, J. Liu, S. Zuo, U.A. Khan, Y. Yu, B. Li, *Appl. Surface Sci.* 444 (2018) 177–186.
- [11] L. Chen, R. Huang, M. Xiong, Q. Yuan, J. He, J. Jia, M.-Y. Yao, S.-L. Luo, C.-T. Au, S.-F. Yin, *Inorg. Chem.* 52 (2013) 11118–11125.
- [12] T. Su, Q. Shao, Z. Qin, Z. Guo, Z. Wu, *ACS Catal.* 8 (2018) 2253–2276.
- [13] H. Li, J. Li, Z. Ai, F. Jia, L. Zhang, *Angew. Chem.* 57 (2018) 122–138.
- [14] S. Tiewcharoen, C. Warakulwit, V. Lapeyre, P. Garrigue, L. Fourier, C. Elissalde, S. Buffière, P. Legros, M. Gayot, J. Limtrakul, A. Kuhn, *Angew. Chem.* 56 (2017) 11431–11435.
- [15] H. Yin, X. Chen, G. Li, Y. Chen, W. Wang, T. An, P.K. Wong, H. Zhao, *Appl. Catal. B Environ.* 245 (2019) 698–705.
- [16] R. He, D. Xu, B. Cheng, J. Yu, W. Ho, *Nanoscale Horiz.* 3 (2018) 464–504.
- [17] H. Li, Y. Zhou, W. Tu, J. Ye, Z. Zou, *Adv. Funct. Mater.* 25 (2015) 998–1013.
- [18] A.D. Liyanage, S.D. Perera, K. Tan, Y. Chabal, K.J. Balkus, *ACS Catal.* 4 (2014) 577–584.
- [19] Y. Huang, H. Li, M.-S. Balogun, W. Liu, Y. Tong, X. Lu, H. Ji, *ACS Appl. Mater. Interfaces* 6 (2014) 22920–22927.
- [20] L. Chen, J. He, Q. Yuan, Y. Liu, C.-T. Au, S.-F. Yin, *J. Mater. Chem. A Mater. Energy Sustain.* 3 (2015) 1096–1102.
- [21] Z. Jiang, X. Liang, H. Zheng, Y. Liu, Z. Wang, P. Wang, X. Zhang, X. Qin, Y. Dai, M.-H. Whangbo, B. Huang, *Appl. Catal. B Environ.* 219 (2017) 209–215.
- [22] Y. He, L. Zhang, B. Teng, M. Fan, *Environ. Sci. Technol.* 49 (2015) 649–656.
- [23] X. Li, T. Wan, J. Qiu, H. Wei, F. Qin, Y. Wang, Y. Liao, Z. Huang, X. Tan, *Appl. Catal. B Environ.* 217 (2017) 591–602.
- [24] X. Xiao, J. Wei, Y. Yang, R. Xiong, C. Pan, J. Shi, *ACS Sustain. Chem. Eng.* 4 (2016) 3017–3023.
- [25] Y. Huang, H. Lu, Y. Lin, Y. Mao, G. Ouyang, H. Liu, S. Zhang, Y. Tong, *J. Mater. Chem. A Mater. Energy Sustain.* 6 (2018) 24740–24747.
- [26] P.-Y. Kuang, J.-R. Ran, Z.-Q. Liu, H.-J. Wang, N. Li, Y.-Z. Su, Y.-G. Jin, S.-Z. Qiao, *Chem. Eur. J.* 21 (2015) 15360–15368.
- [27] P. Madhusudan, J. Ran, J. Zhang, J. Yu, G. Liu, *Appl. Catal. B Environ.* 110 (2011) 286–295.
- [28] X. Chang, T. Wang, P. Zhang, J. Zhang, A. Li, J. Gong, *J. Am. Chem. Soc.* 137 (2015) 8356–8359.
- [29] Y. Huang, H. Xu, H. Yang, Y. Lin, H. Liu, Y. Tong, *ACS Sustainable Chem. Eng.* 6 (2018) 2751–2757.
- [30] H. Liu, H.T. Ma, X.Z. Li, W.Z. Li, M. Wu, X.H. Bao, *Chemosphere* 50 (2003) 39–46.
- [31] J. Kong, G. Li, M. Wen, J. Chen, H. Liu, T. An, *J. Catal.* 370 (2019) 88–96.
- [32] M. Zeng, Y. Li, M. Mao, J. Bai, L. Ren, X. Zhao, *ACS Catal.* 5 (2015) 3278–3286.
- [33] F.-X. Xiao, M. Pagliaro, J.-Y. Xu, B. Liu, *Chem. Soc. Rev.* 45 (2016) 3088–3121.
- [34] Y. Hou, F. Zuo, A.P. Dagg, J. Liu, P. Feng, *Adv. Mater.* 26 (2014) 5043–5049.
- [35] Y. Huang, B. Long, M. Tang, Z. Rui, M.-S. Balogun, Y. Tong, H. Ji, *Appl. Catal. B Environ.* 181 (2016) 779–787.
- [36] D. Jiang, W. Wang, L. Zhang, Y. Zheng, Z. Wang, *ACS Catal.* 5 (2015) 4851–4858.
- [37] C. Karunakaran, P. Gomathisankar, *ACS Sustainable Chem. Eng.* 1 (2013) 1555–1563.
- [38] X. Pan, M.-Q. Yang, X. Fu, N. Zhang, Y.-J. Xu, *Nanoscale* 5 (2013) 3601–3614.
- [39] Z. Liu, T. Lu, T. Song, X.-Y. Yu, X.W. Lou, U. Paik, *Energy Environ. Sci.* 10 (2017) 1576–1580.
- [40] K. Ye, K. Li, Y. Lu, Z. Guo, N. Ni, H. Liu, Y. Huang, H. Ji, P. Wang, *Trends Analyt. Chem.* 116 (2019) 102–108.
- [41] F. Ning, M. Shao, S. Xu, Y. Fu, R. Zhang, M. Wei, D.G. Evans, X. Duan, *Energy Environ. Sci.* 9 (2016) 2633–2643.
- [42] C.R. Wang, K.B. Tang, Q. Yang, Y.T. Qian, *Chem. Phys. Lett.* 357 (2002) 371–375.
- [43] J. Duan, S. Chen, M. Jaroniec, S.Z. Qiao, *ACS Nano* 9 (2015) 931–940.
- [44] H. Xu, Y. Hu, D. Huang, Y. Lin, W. Zhao, Y. Huang, S. Zhang, Y. Tong, *ACS Sustainable Chem. Eng.* 7 (2019) 5784–5791.
- [45] R. Marschall, *Adv. Funct. Mater.* 24 (2014) 2421–2440.
- [46] X. Wang, F. Wang, Y. Sang, H. Liu, *Adv. Energy Mater.* 7 (2017) 1700473–1700488.
- [47] Z. Jiang, W. Wan, H. Li, S. Yuan, H. Zhao, P.K. Wong, *Adv. Mater.* 30 (2018)

- 1706108–1706117.
- [48] L. Zhu, H. Li, P. Xia, Z. Liu, D. Xiong, *ACS Appl. Mater. Interfaces* 10 (2018) 39679–39687.
- [49] J. Cheng, J. Feng, W. Pan, *ACS Appl. Mater. Interfaces* 7 (2015) 9638–9644.
- [50] J.J.M. Vequizo, H. Matsunaga, T. Ishiku, S. Kamimura, T. Ohno, A. Yamakata, *ACS Catal.* 7 (2017) 2644–2651.
- [51] M.J. Muñoz-Batista, M. Fernández-García, A. Kubacka, *Appl. Catal. B Environ.* 164 (2015) 261–270.
- [52] J.L. Gunjakar, T.W. Kim, H.N. Kim, I.Y. Kim, S.-J. Hwang, *J. Am. Chem. Soc.* 133 (2011) 14998–15007.
- [53] F. Dong, Z. Zhao, T. Xiong, Z. Ni, W. Zhang, Y. Sun, W.-K. Ho, *ACS Appl. Mater. Interfaces* 5 (2013) 11392–11401.
- [54] Y. Huang, K. Li, Y. Lin, Y. Tong, H. Liu, *ChemCatChem* 10 (2018) 1982–1987.
- [55] T. Su, Z.D. Hood, M. Naguib, L. Bai, S. Luo, C.M. Rouleau, I.N. Ivanov, H. Ji, Z. Qin, Z. Wu, *Nanoscale* 11 (2019) 8138–8149.
- [56] N. Wetchakun, S. Chaiwichain, B. Inceesungvorn, K. Pingmuang, S. Phanichphant, A.I. Minett, J. Chen, *ACS Appl. Mater. Interfaces* 4 (2012) 3718–3723.
- [57] M.S. Ansari, A. Banik, M. Qureshi, *Carbon* 121 (2017) 90–105.